HOKKAIDO UNIVERSITY

Title	Verification of three-dimensional retrieval of microphysical and thermodynamic variables in snow cloud using ARPS numerical model
Author(s)	Sun, Shouxiang; UYEDA, Hiroshi
Citation	Journal of the Faculty of Science, Hokkaido University. Series 7, Geophysics, 11(5), 773-791
Issue Date	2001-03-26
Doc URL	http://hdl.handle.net/2115/8862
Type	bulletin (article)
File Information	11(5)_p773-791.pdf

Instructions for use

Verification of Three-Dimensional Retrieval of Microphysical and Thermodynamic Variables in Snow Cloud Using ARPS Numerical Model

Shouxiang Sun* and Hiroshi Uyeda**

*Division of Earth and Planetary Sciences, Graduate School of Science,
Hokkaido University, Sapporo 060-0810, Japan*

(Received December 15, 2000)

Abstract

We improved the algorithm developed by Roux (1988) to make it appropriate for
snow clouds and applied the improved algorithm to the case observed in Ishikari Bay,
Hokkaido in 1992. The results were verified by using Advanced Regional Prediction
System (ARPS). The ARPS numerical model was used to generate fields of wind and
water components with the sonde data obtained by Keifumaru, research vessel, as
base status. The three-dimensional perturbation of pressure and potential tempera-
ture were retrieved with these fields. The retrieved perturbation fields were compar-
ed with the output of ARPS run. The confirmation study using ARPS made sure that
a) the algorithm gives reasonable result, b) it is necessary to calculate local changes
with 10-minutes long time interval between consequential radar volume scans.

1. Introduction

Every winter heavy snowfalls hit the west coast area of Japan. In recent
years, multiple Doppler rader observations have been carried out and a large
quantity of Doppler and sonde data have been recorded. However, when
studying these snow clouds, researchers usually analyze only wind fields and
radar reflectivity factors and their relationships. We think that it is insufficient
without studying the dynamic structures in snow clouds.

Over the past two decades, many researchers have studied the retrieval of
microphysical and thermodynamic variables in clouds using wind fields comput-
ed from Doppler observation data. Gal-Chen (1978) suggested an algorithm to
permit an unique determination of density and pressure perturbations. Hane

---

* Present affiliation : Access Corporation, Jinbo Cho Kyowa Building 7F, 1-64 Kanda
   Jinbo Cho, Chiyoda Ku, Tokyo 101-0051, Japan.
** Present affiliation : IHAS, Nagoya Univ., Nagoya 464-8601, Japan.

and Scott (1978) made 2D retrieval test for determining temperature and pressure perturbations within convective clouds using data generated by a 2D numerical cloud model. Hane and Ray (1985) retrieved horizontal pressure and buoyancy fields from Doppler radar data in a tornadic thunderstorm. Many researchers also studied three-dimensional retrieval algorithms. For example, Roux (1985) employed simple parameterization for warm cloud physical processes to estimate the criterion at each vertical layer and added them to the 2D perturbation fields. Roux (1988), Roux and Sun (1990) made tests using the same parameterizations as Roux (1985), but they retrieved the 3D temperature perturbation and 3D pressure perturbation with 3D functionals. Hauser et al. (1988) employed mass continuity equations of total water substance, water vapor, and precipitations water in addition to the momentum and thermo-dynamic equations. Marécal et al. (1993) retrieved the microphysical variables in a narrow cold-frontal rainband with detailed parameterization of microphysical processes, including ice-phase processes.

We implemented 3D retrievals using data observed from two Doppler radars in January 23, 1992. In our algorithm, a complete set of governing equations were used and ice-phase microphysical processes were taken into account. Details are given in our another paper (Sun and Uyeda, 2001).

To make such retrievals, however, it is necessary to calculate the horizontal gradients of pressure and temperature fields. One disadvantage of Doppler observation is that it requires a relatively long time, typically three to five minutes for one volume scan. Furthermore, the time interval between two consecutive volume scans is usually even longer. Such long scanning times and intervals make it difficult to correct the advective effect during one volume scan and to calculate local changes in wind components. Because of the rapid changes in meso-scale systems, things become even more complicated, especially for individual precipitation cells. Sun and Houze (1991) applied the retrieval technique developed by Roux and Sun (1990) to a numerical model and suggested that the time resolution of the wind fields should be less than two minutes. However, his conclusion was drawn based on internal consistencies. According to Hane and Ray (1985), internal consistencies are not absolute standards. Roux et al. (1984) studied a case computing local change terms in a time interval of six minutes. He argued that the characteristic variation time of the squall line was 28.6 minutes, as discussed by Chong et al. (1983), and the wind fields appeared stationary in the moving reference frame. Therefore, to calculate the local changes in six minute intervals was no problem. Nevertheless, Hauser et al. (1988) studied the same case while rejecting local changes. It

seems there is no big difference in their results.

As different researchers dealt with this problem in different ways, even for the same case, we think it is necessary to make tests to confirm whether it is necessary and feasible to calculate the local changes of wind fields with long time intervals. The verification test was made using the ARPS (Advanced Regional Prediction System, developed by researchers at the University of Oklahoma, Xue et al., 1995) numerical model. In this paper, we describe the results of our ARPS confirmation study.

2. Purpose of the Verification

The version of ARPS that we used, 4.2.4, is capable of simulating a cloud system. Surface heat and moisture fluxes and soil model are included in the model. The six-component (water vapor, cloud water, cloud ice, rain, snow, and graupel) ice-phase microphysical processes are also included. Because this model is in public domain we used it to verify our retrieval algorithm and to look for useful guides for implementing actual retrievals.

First, we want to point out that cloud models usually cannot predict or simulate the development of precipitation clouds in all cases. This is due to our limited understanding of the exact physical processes in clouds and also because of the lack of accurate initial fields. Also bias of predicted fields from actual fields increases during the process of integration. Because Doppler radar can observe the reflectivity and Doppler velocity of air in clouds, it is interesting and important to study the retrieval of non-observed fields using observed fields.

As both the cloud model and the retrieval algorithm use the same set of governing equations of air movement (ARPS uses a different formula from that used in our retrieval algorithm to calculate net buoyancy), it is at least possible to use the model's output to verify the effect of our retrieval.

The purposes of our verification are 1) to confirm whether the retrieval is reliable and, 2) to confirm whether it is necessary to calculate local change terms with consecutive radar observations in 10-minute intervals.

The first point is important because it shows whether the retrieval algorithm and programs are right. The second point is also important because in our observations, a 10-minute interval is adopted during two consecutive volume scans. This duration may be too long, so we study it with the ARPS model to determine if it is acceptable. It is necessary to make this confirmation because the individual snow cells usually do not satisfy the steady assumption.

3. Numerical Test

A numerical test was implemented using the sonde profile observed by the Keifu-maru vessel in the Japan Sea, west of Ishikari Bay, Hokkaido, at 0830 JST on January 23, 1992 (as shown in Fig. 1).   The sonde data show that at the altitude of 3 m the relative humidity was 98%, while at 59 m, the relative humidity was 54%.   From 59 m to 700 m the relative humidity increased rapidly, reaching 88% at 696 m.   This feature causes the lapse rate of equivalent potential temperature to decrease from 59 m until 700 m.   The stratification was therefore unstable for the saturated air.   Because the relative humidity is very high at altitudes below 59 m, the air soon becomes saturated whenever there is a weak disturbance that causes an updraft.   However one should note that from 3,000 m to 5,000 m the equivalent potential temperature increased rapidly.   This is why the top of the snow cell we studied is at about 3,500 m.

The convection is activated with a warmer bubble.   No terrain is included because we simulate the snow cloud above the sea.   Table 1 shows some of the parameters used in the simulation.

Figure 2 shows 14 cross-sections of the mixing ratios of precipitating ice (snow and graupel).   Snow and graupel were added together in our retrieval
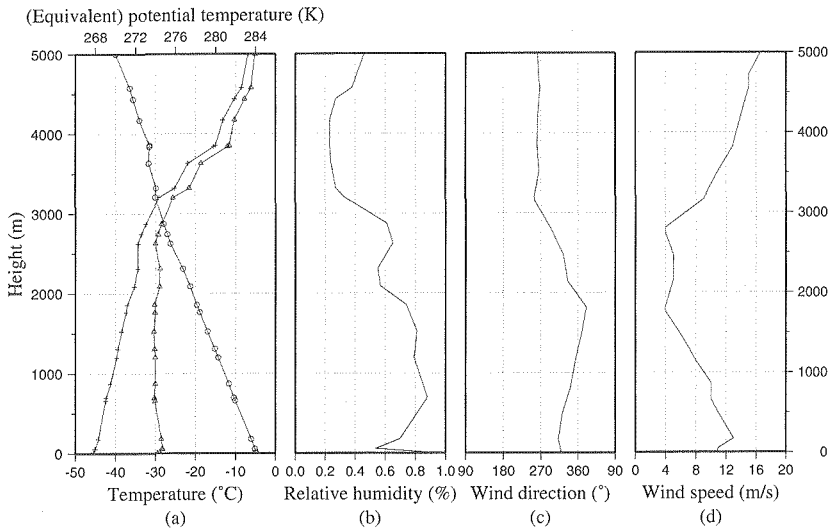

Fig. 1.   The sonde profiles.   (a) temperature (°C, circles), potential temperature (K, crosses) and equivalent potential temperature (K, triangles), (b) relative humidity (%), (c) wind direction (°), (d) wind speed (m·s^{-1}).   The vertical axis shows height (m).

Table 1.   Main parameters used in the snow simulation.

grid system	number of grids	$61 \times 61 \times 21$
	horizontal grid length	1,000 m
	vertical grid length	250 m
initial bubble	horizontal radius	10,000 m
	vertical radius	1,000 m
	center coordinates	(20,000 m, 50,000 m, 0 m)
	magnitude	4K
time steps	big step	5 s
	small step	0.5 s
boundary condition	lateral boundary	radiation (Klemp-Lilly/Durran (1983))
	bottom boundary	rigid wall
	top boundary	rigid wall
turbulence	implementation	1.5 order TKE mixing
moist progresses	scheme	Paul Schultz's (FSL) scheme (1995)
	components	water vapor, cloud water, rain cloud ice, snow, graupel

algorithm because it is virtually impossible to distinguish them in conventional Doppler observations.   The simulated snow cloud can be found at 20 min.   Its intensity increases and reaches a maximum at 35 min.   The maximum mixing ratio was larger than 5×10^{-4} kg $\cdot$ kg^{-1}.   After 35 min. the intensity began to decrease and finally only a small area where the mixing ratio was lower than 5×10^{-5} kg $\cdot$ kg^{-1} was left at 85 min.   As shown in the figure, the simulated snow moved toward the southeast, its center moved to the right, and the y value decreased.

4.   Comparison of Retrieved Fields and ARPS output

Tests were made using the model's wind and water component fields to retrieve the perturbations of pressure and potential temperature.   Besides the summed mixing ratio of snow and graupel, the model's fields of mixing ratios of water vapor, cloud water, and cloud ice were also used for all the tests.   This was because the model uses different parameterization schemes of microphysics than our retrieval algorithm.   But note that for calculating the heat source and sink, our parameterization schemes were still used.

The perturbations of pressure and potential temperature derived from ARPS output were defined as

$$v_1' = v - \bar{v}, \quad v_1 = v_1' - \bar{v_1'},$$

were v denotes the ARPS output value, which is pressure or potential tempera-
ture; $\bar{v}$ is the base state value; v_1' is the horizontal perturbation; and v_1 is the
perturbation with the 3D averaged value $\bar{v_1'}$ subtracted, which means the net
perturbation in the 3D retrieval domain is reset to zero.

For the retrieval implemented here, all the lateral boundaries for θ_a and Π_1
were set as Neumann condition. The precision of iteration was 1×10^{-5} for the
former and 1×10^{-6} for the latter. The system moving speeds were derived
from the shift of the centers of gravity of the snow mixing ratio fields at two
selected time levels. The x and y coordinates of the centers of gravity were
defined as

$$x_c = \frac{\sum q_s x}{\sum q_s}, \quad y_c = \frac{\sum q_s y}{\sum q_s}.$$

4.1. Mature Stage

We first give the results of a test which used the ARPS output at 40 min. and
30 min. in order to confirm the reliability of using the 10-minute interval. As
shown in Fig. 2, the simulated snow cloud was the strongest at 35 min. indicating
that this test corresponds to the mature stage.

a) Perturbation Fields Derived From ARPS Output

The horizontal pressure perturbation patterns at altitudes of 500 m, 1,000 m,
1,500 m, 2,000 m, 2,500 m and 3,000 m, derived from the ARPS output, are shown
in Figs. 3 and 4. The potential temperature patterns are shown in Figs. 5 and
6.

As shown in the figures, the pressure perturbation patterns mainly feature
positive values in the right and negative values in the left at low levels. This
pattern turns clockwise with the altitude increasing and at 2,000 m, 2,500 m, and
3,000 m levels the positive area is in the south half while the negative area is in
the north half. There are positive centers at about (37.5 km, 32 km) at altitudes
of 500 m and 1,000 m. To the left of the positive centers, negative ones are
visible. If we connect the positive and negative centers with a line, we observe
that the line rotates clockwise as the pattern gains altitude. In Fig. 4(c) the
positive center has moved to the left and the negative one has moved to the
right.

As shown in Fig. 5(a), the shape of a warm bubble is still visible at 40 min.
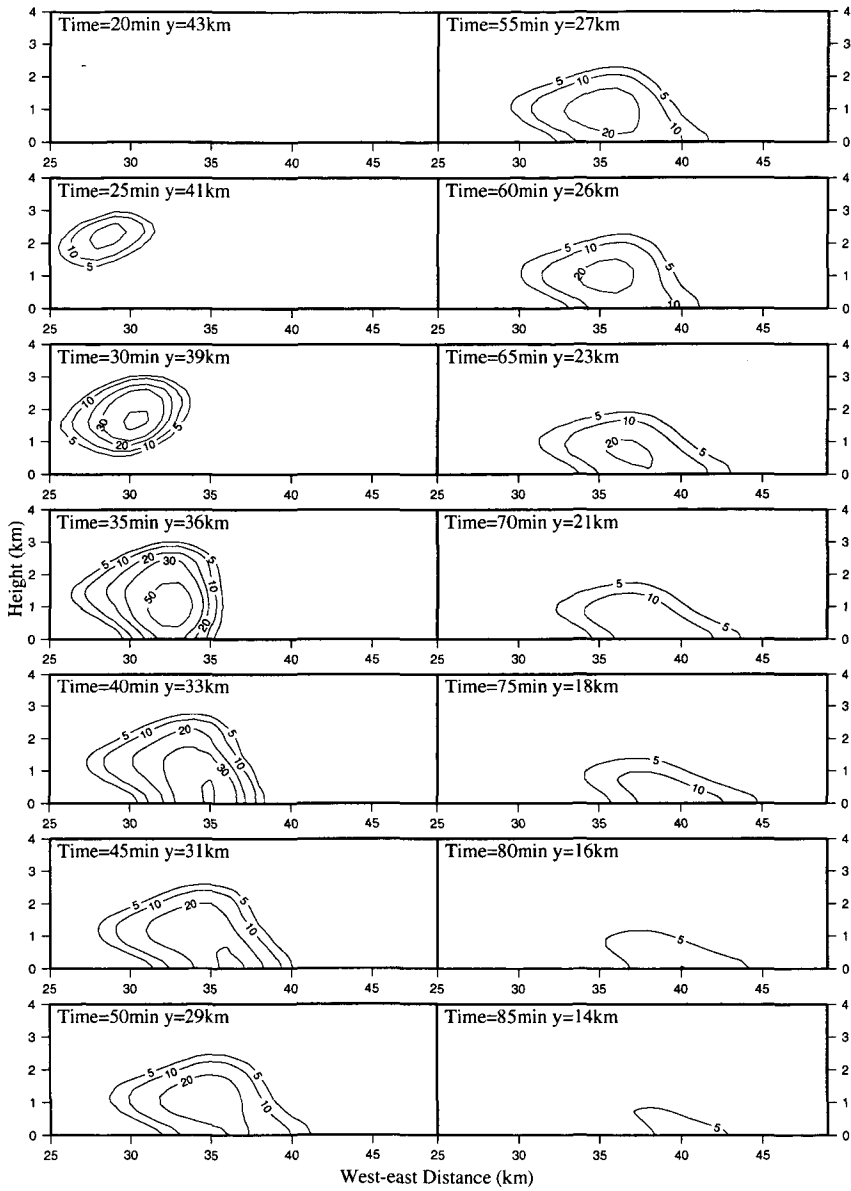However to the left of the center of the domain a relatively cold area can be

Fig. 2. The sum mixing ratios of snow and graupel (10^{-5} kg · kg^{-1}) at different time levels simulated by ARPS. y value denotes where the cross-section is made.
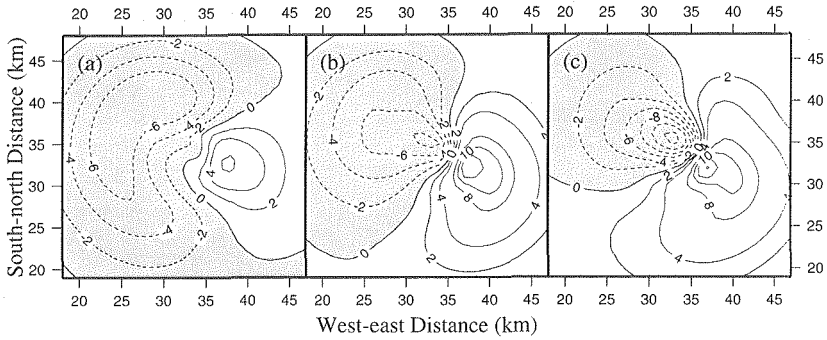
Fig. 3. Pressure perturbation (Pa) derived from ARPS output at the altitude of (a) 500 m, (b) 1,000 m and, (c) 1,500 m at 0040 min.
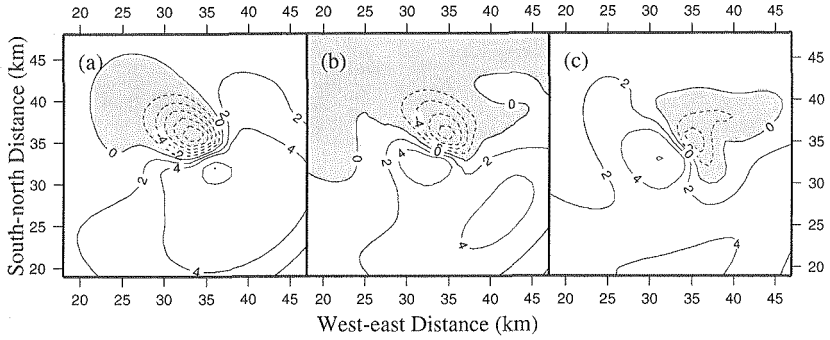

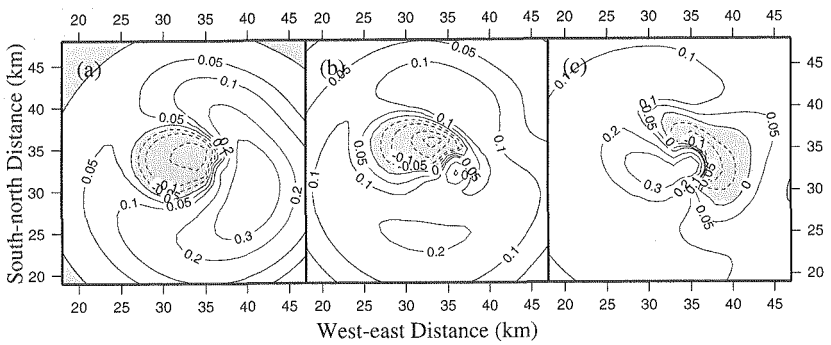Fig. 4. Same as Fig. 3 but for (a) 2,000 m, (b) 2,500 m and, (c) 3,000 m.

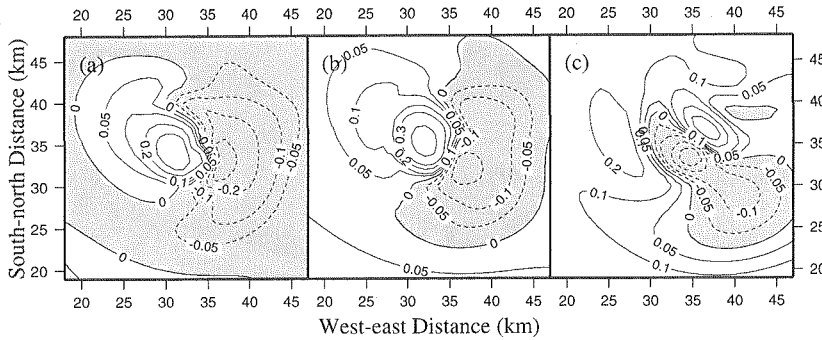Fig. 5. Same as Fig. 3 but for perturbation of potential temperature (K).

Fig. 6.   Same as Fig. 5 but for (a) 2,000 m, (b) 2,500 m and, (c) 3,000 m.

found.   A warmer center also exists to its right.   Again, the axis that linked the two centers turns clockwise while the altitude increases, though more rapidly than it does in the pressure pattern.   The pattern shown in Fig. 6(c) is more complex than those at lower levels.   In this figure the positive core is separated by the negative one.

b) Comparison between Local Change, Advection and Turbulence

The root mean squares of local changes, advections, and turbulent stresses in x, y and z directions are listed in Table 2.   From this table we can see that local change terms in the x and y directions are generally smaller than advective ones.   However, since they are in the same order, ignoring the local changes might cause a greater error.   Whereas in the vertical direction the advective terms are smaller than the local changes.   On the other hand, the turbulent

Table 2.   Root-mean-squares (10^{-4}m $\cdot$ s^{-2}) of local changes, advections and turbulent stresses in u, v and w equations at different layers for 40 min. calculated from the ARPS output at 30 min. and 40 min.   *Lcl, Adv* and *Tur* denote local change, advection and turbulence respectively.

Layer (m)	x			y			z		
	Lcl	*Adv*	*Tur*	*Lcl*	*Adv*	*Tur*	*Lcl*	*Adv*	*Tur*
500	4.77	7.05	0.68	4.40	3.62	0.14	1.78	1.42	0.16
1,000	6.08	10.80	0.53	4.17	6.32	0.59	2.77	2.17	0.31
1,500	7.49	11.34	0.84	5.38	11.66	0.46	3.41	2.28	0.42
2,000	5.47	7.44	0.38	4.72	7.33	0.34	3.66	2.30	0.19
2,500	4.67	4.65	0.18	5.55	7.61	0.17	2.88	2.13	0.21
3,000	4.89	9.07	0.13	4.86	8.91	0.21	1.74	3.92	0.06

Table 3. Same as Table 2 but calculated from the ARPS output at 35 min. and 40
          min.

Layer (m)	x			y			z		
	Lcl	Adv	Tur	Lcl	Adv	Tur	Lcl	Adv	Tur
500	6.57	8.83	0.68	4.51	4.94	0.14	2.10	1.66	0.16
1,000	6.06	10.60	0.53	5.07	6.26	0.59	3.26	2.10	0.31
1,500	6.03	9.71	0.84	5.28	10.73	0.46	3.68	1.56	0.42
2,000	4.33	5.97	0.38	4.22	6.07	0.34	3.47	1.82	0.19
2,500	3.85	4.64	0.18	4.88	7.43	0.17	2.54	2.30	0.21
3,000	4.01	9.67	0.13	4.44	8.77	0.21	1.38	4.60	0.06

Table 4. Same at Table 2 but calculated from the ARPS output at 39 min. and 40
          min.

Layer (m)	x			y			z		
	Lcl	Adv	Tur	Lcl	Adv	Tur	Lcl	Adv	Tur
500	18.31	19.17	0.68	12.95	14.71	0.14	2.75	2.84	0.16
1,000	26.89	27.26	0.53	18.71	18.99	0.59	5.82	5.31	0.31
1,500	25.91	23.93	0.84	12.56	15.38	0.46	9.96	7.17	0.42
2,000	12.36	10.89	0.38	12.16	7.51	0.34	9.61	6.54	0.19
2,500	8.64	7.34	0.18	11.67	6.81	0.17	6.13	4.41	0.21
3,000	8.00	12.15	0.13	7.66	7.36	0.21	3.59	3.11	0.06

terms are very small compared with the other two and are therefore negligible.
This is because the ARPS generated very small turbulent viscosity coefficients.

The root mean squares were also calculated using the ARPS output pairs
(35 min., 40 min.) and (39 min., 40 min.), which are in 5 min. and 60 sec. intervals
respectively.   The results are shown in Tables 3 and 4.   For the 5-min. interval
pair, system moving speeds of 3.333 m·s⁻¹ (Us) and −6.667 m·s⁻¹ (Vs) were used.
For the 60-sec. pair, the original wind fields were used instead of the cell relative
ones because during the one-minute interval the simulated cloud did not move
by more than one grid either in the x or y directions.   Therefore, the result
obviously differs from that shown in Table 2.   These three tables show that the
local change terms are comparable with the advective terms, and are thus
important for the retrieval.   Comparing Table 2 and Table 3, we also find that
calculating the local changes with a 5-min. interval or with a 10-min. interval
does not make any obvious change in the relative importance of local change
terms and advective terms.

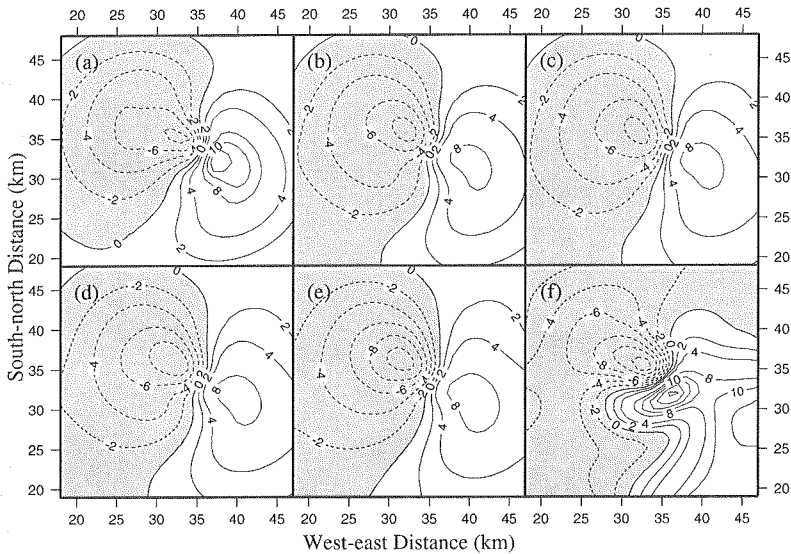To illustrate this more clearly, we show the retrieved 2D pressure perturba-

Fig. 7. 2D pressure perturbation (Pa) at 1,000 m level at 40 min. retrieved with different time intervals. (a) ARPS output, (b) 5 seconds, (c) 1 minutes, (d) 5 minute, (e) 10 minutes, and (f) steady (no local changes). The contours are in a interval of 2.

tion at 1,000 m level with different time intervals in Fig. 7.

We can ascertain from this figure that, generally speaking, different time intervals do not appreciably affect the results. They all are a little different from the ARPS output. This difference is induced during solving the Euler equations. However, change is apparent if we exclude local change terms of wind components. Therefore, while it is necessary to calculate local changes, doing so over a long interval (e.g., 10 minutes) does not matter significantly.

We show the turbulent viscosity coefficient for momentum in Fig. 8. We found that in all layers, turbulence only exists in convective areas. The maximum K_m was about 80 m²s⁻¹. This can be considered rather small compared with the values used in Hauser et al. (1988) and Marécal et al. (1993). The root mean square values listed in the above tables are understimated because they are calculated in the whole domain. However, even if they were calculated only in the convective areas, such small K_m values would not make the turbulent forces comparable with advections or local changes. In a word, turbulent stresses are relatively small and can be ignored.
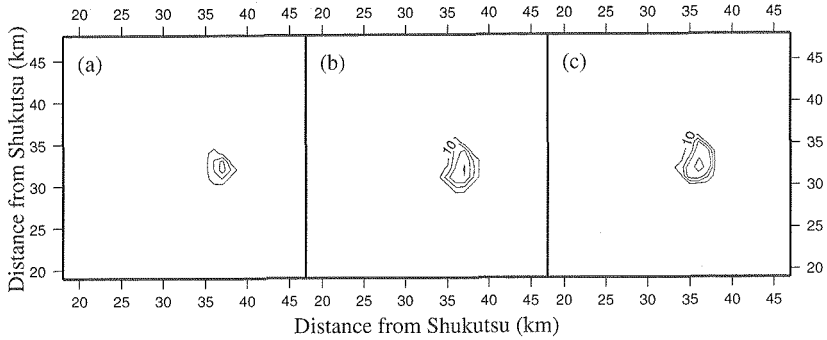
Fig. 8.   Turbulent viscosity coefficient for momentum (m²s⁻¹) at (a) 500 m, (b) 1,000 m
         and, (c) 1,500 m at 0040 min.   The contour levels are 10, 30, 50, 80.

c)   Retrieved Perturbation Fields

For the retrieval at 40 min., the system moving speeds U_s and V_s are set respectively as 4.975 m·s⁻¹ and -7.327 m·s⁻¹ and were reset to 5.000 m·s⁻¹ and -6.667 m·s⁻¹ to keep accordance with the moving coordinate system.

The retrieved perturbation fields are shown in Figs 9, 10, 11 and 12. Comparing them with the ARPS fields, we find that they are in good agreement, although there are some shifts in values and changes in shapes.   The positions of the centers match well, but the pressure patterns are better than the potential temperature ones.   Studying Figs. 11(c) and 12(c), we find relatively large nega- tive areas.   And for Fig. 12(c), the negative area is not spatially continuous.   A small negative area exists to the north of the right positive core.   Nevertheless, the contour 0 in Fig. 12(c) matches well with the contour 0.1 in Fig. 6(c). Similarly, if we subtract 0.1 from the perturbation shown in Fig. 5(c) we find the
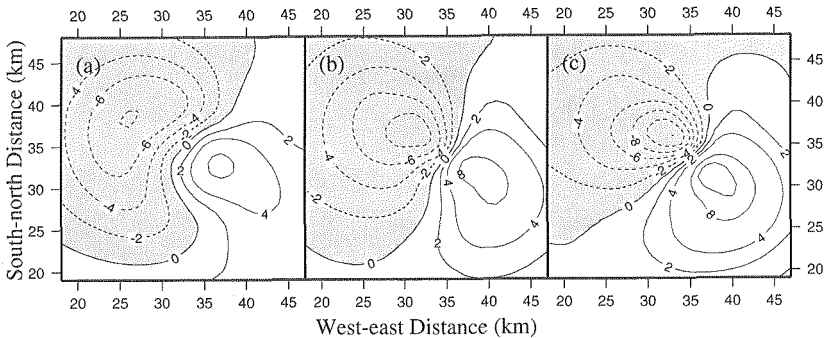
Fig. 9.   Same as Fig. 3 but retrieved with ARPS output at 30 min. and 40 min.
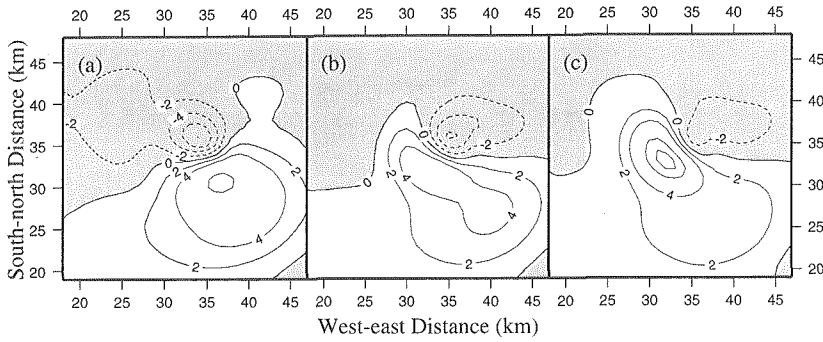
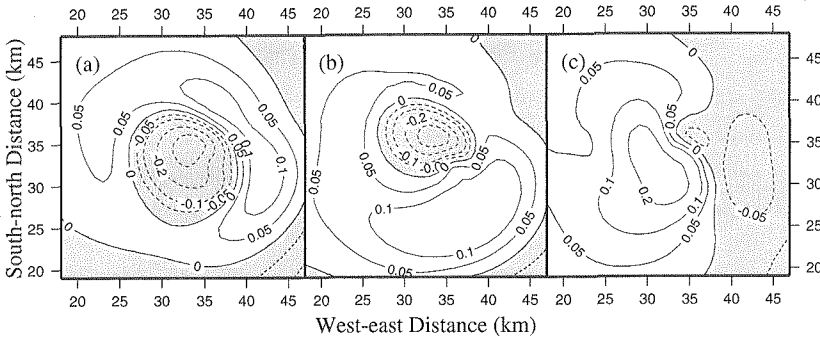Fig. 10.   Same as Fig. 9 but for (a) 2,000 m, (b) 2,500 m and, (c) 3,000 m.

Fig. 11.   Same as Fig. 9 but for perturbation of potential temperature (K).
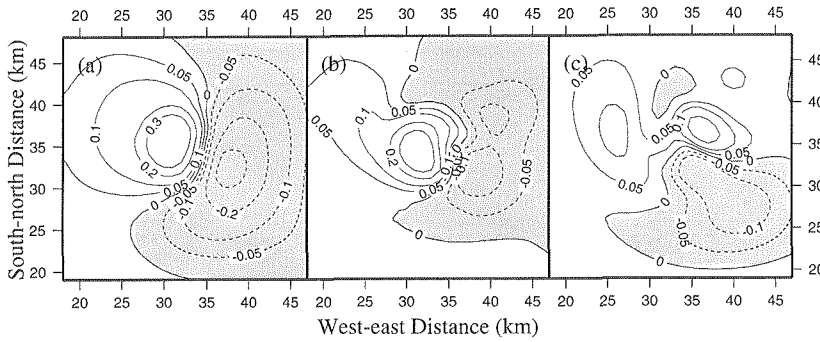
Fig. 12.   Same as Fig. 11 but for (a) 2,000 m, (b) 2,500 m and, (c) 3,000 m.

negative area is rather consistent with that shown in Fig. 11(c).   Such shifts are caused by the different ways of computing the perturbation.   However, exclusion of this shift does not improve the result at all levels, as can be seen in Figs.

6(a) and 12(a), which indicate a different scenario. Moreover, the figures of the pressure perturbation do not seem to have an identical shift between the ARPS and the retrieved fields. Nevertheless, we should find that the patterns of the retrieved fields, and the places and intensities of the perturbation cores, are still quite satisfactory.

d) Comparison in Vertical Direction

The vertical profiles of the maximum and minimum perturbations are shown in Fig. 13. Generally speaking, the results is good enough because the lines of ARPS output and retrieved fields are in accordance with each other, except where there are relatively noticeable differences in temperature perturbation at layers lower than 1,000 m.

In our view, the perturabation patterns we have introduced above indicate that retrieval using radar volume scan data with a 10-minute interval is possible and reliable. To confirm this we drew two vertical cross-sections of perturbations for the ARPS output and the retrieved fields in order to check whether the vertical patterns matched well. The cross-sections are shown in Figs. 14 and 15.

As shown in Fig. 14, the main features of the pressure perturbation are 1) a large area of negative perturbation exiting from 18 km to 35 km in the x direction below 2,000 m, with its core at (24 km, 0.4 km) ; 2) to the right of the negative area a positive area with its core at (37.5 km, 1 km), extending to the bottom of the negative area ; 3) a positive left half above 2,000 m ;
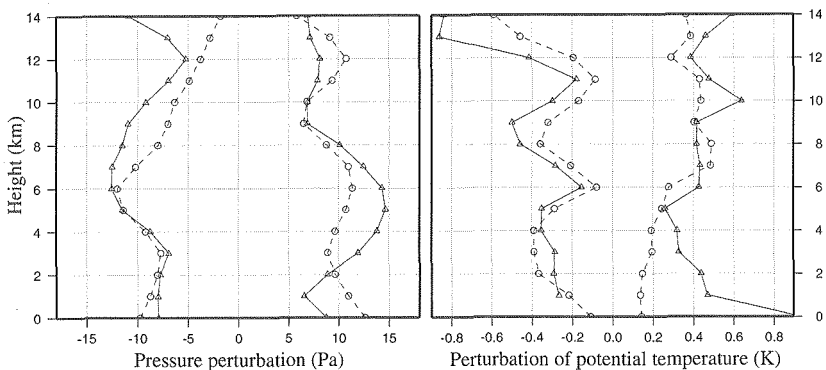

Fig. 13. Vertical profiles of the maximum and minimum perturbations of pressure (left) and those of potential temperature (right). The solid lines are for the ARPS output and the dashed ones are for the retrieved fields.
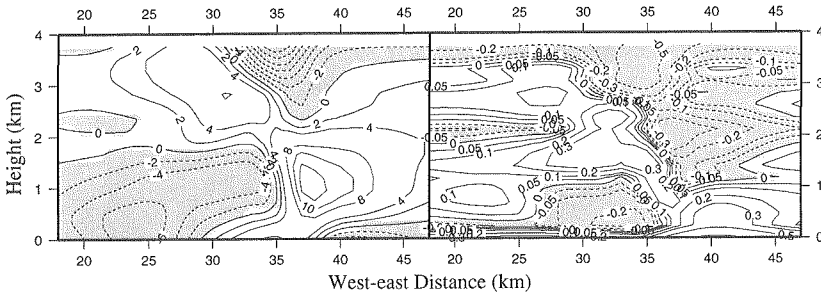
Fig. 14.   Vertical cross-sections of perturbation of pressure (left) and that of potential temperature (right) derived from ARPS output at 40 min. $y = 33$ km.
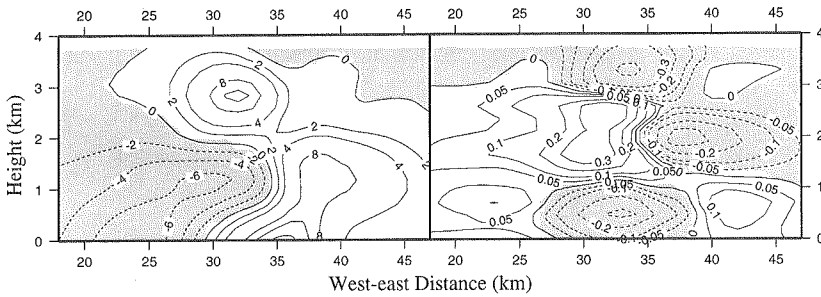

Fig. 15.   Same as Fig. 14 but retrieved with ARPS output at 30 min and 40 min.

and 4) a negative right half above 2,000 m.   The main features of the perturbation of potential temperature are 1) below 1,000 m, from left to right in the x direction, a positive perturbation area, then a negative area, then a positive area again, (each block of perturbation is nearly the same size in the x direction as the others; 2) above 1,000 m and below 2,500 m, perturbation changing from negative to positive and then negative again until the right boundary and; 3) above 2,500 m, in the middle of the domain, a negative core.   Almost all of these features are recovered in the retrieval, as shown in Fig. 15, with the exception of the negative pressure perturbation above 2,500 m and the negative temperature perturbation at the middle layer and in the left part, which are not visible.   In spite of this, we think the retrieval revealed the original perturbation characteristics very well.

4.2.   Dissipating Stage

To verify the retrieval algorithm for the dissipating stage, we made another retrieval using the ARPS output at 50 min. and 60 min.   The

perturbation fields of pressure and potential temperature generated by the ARPS model are shown in Fig. 16 and 17 for the altitudes of 500 m, 1,000 m, and 1,500 m. System moving speeds U_s and V_s were set respectively at 3.333 m•s^{-1} and -6.667 m•s^{-1}.

In Fig. 16(a), the pressure perturbation pattern features a round-shaped positive are in the right part. Negative centers can be found at about (37 km, 28 km) in Figs. 16(b) and 16(c) with a large part of positive perturbation left. At 500 m level, as shown in Fig. 17(a), is a relatively cold area at the center of the domain, with an obvious warm area to the southeast. This area of cold perturbation shrinks at 1,000 m, and to its south a warm core. At 1,500 m, the perturbation pattern rotates clockwise.

The retrieved fields are shown in Figs. 18 and 19. The important features in the pressure perturbation patterns were well recovered. The low centers at 1,000 m and 1,500 m and the positive perturbation to their
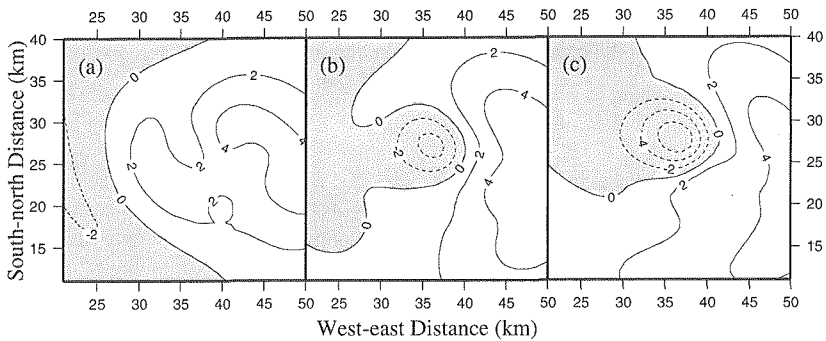

Fig. 16. Pressure perturbation (Pa) derived from ARPS output at the altitude of (a) 500 m, (b) 1,000 m and, (c) 1,500 m at 0060 min.
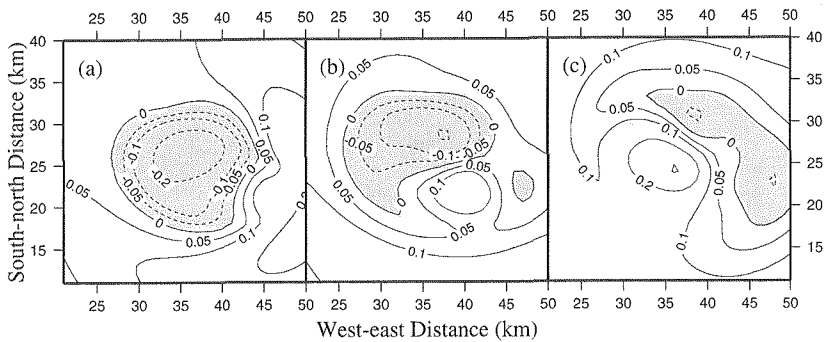

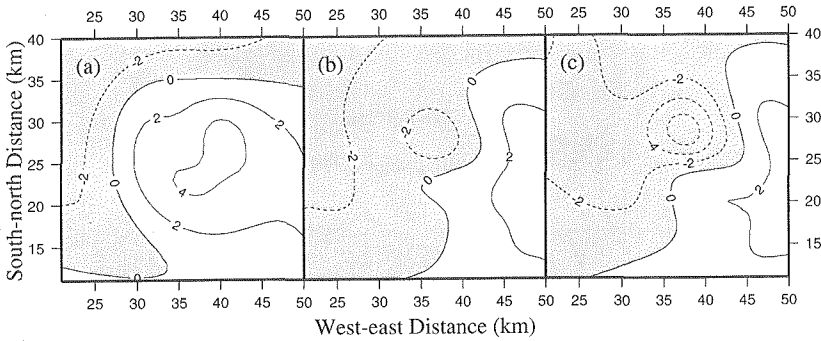Fig. 17. Same as Fig. 16 but for perturbation of potential temperature (K).

Fig. 18.   Same as Fig. 16 but retrieved using the ARPS output at 50 min. and 60 min.
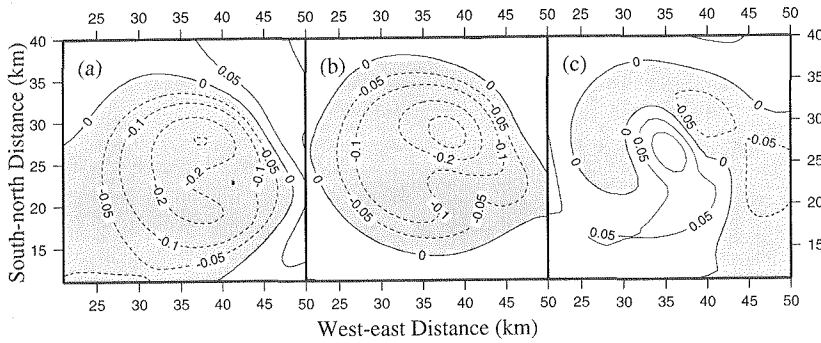

Fig. 19.   Same as Fig. 18 but for perturbation of potential temperature (K).

right are consistent with the ARPS output.   The general situation in Fig. 18(a) is the same as in Fig. 16(a), except that the positive core in Fig. 18(a) actually does not exit in Fig. 16(a).   At first glance, there appears to be more negaftive areas in Fig. 19 than in Fig. 17.   However, we still find that the structure of contours corresponds well to the ARPS output if we remove a negative shift in Fig. 19.   The warmer core to the south of the colder one in Fig. 17(b) was not recovered successfully, but in Fig. 19(b) a relatively warm area, shown by a rising part at about (38 km, 22 km), is still visible.

5.   Conclusion

Using the ARPS numerical model, we conducted a verification test of our algorithm for three-dimensional retrieval of thermodynamic and microphysical variables in snow clouds.   We simulated a snow cell using

the sonde data gathered on January 23, 1992.   Two retrieval tests, one for
the mature stage and one for the dissipating stage, were made and the
perturbation fields were compared with the ARPS output.   The relative
importance of different terms in the momentum equations was discussed.
Our results showed that it is necessary to calculate the local changes of
wind components in order to obtain better effects.   However, a time inter-
val as long as 10 minutes does not seem to be significant.   We believe that
structures rather than values of the fields are of greater importance.
Considering the patterns of perturbation fields and comparing fields
retrieved with different time intervals, we found that it is feasible and
reliable to calculate local changes with wind data in 10-minute time inter-
vals.   Turbulence, on the other hand, is a negligible factor and can be
ignored.

Acknowledgments

References

Chong, M., J. Testud, and F. Roux, 1983.   Three-dimensional wind field analysis from dual-
       Doppler radar data.   Part II: Minimizing the error due to temporal variation.   *J.
       Climate Appl. Meteo.*, **22**, 1216-1226.
Gal-Chen, T., 1978.   A method for the initialization of the anelastic equations: implications
       for the matching models with observations.   *Mon. Wea. Rev.*, **106**, 587-606.
Hane, C.E., and P.S. Ray, 1985.   Pressure and buoyancy fields derived from Dopler radar data

in a tornadic thunderstorm. *J. Atmos. Sci.*, **42**, 18–35.

Hane, C.E., and B.C. Scott, 1978.   Temperature and pressure perturbations within convective clouds derived from detailed air motion information: Preliminary testing. *Mon. Wea. Rev.*, **106**, 654–661.

Hauser, D., F. Roux, and P. Amayenc, 1988.   Comparison of two methods for the retrieval of thermodynamic and microphysical variables from Doppler radar measurements: Application to the case of a tropical squall line. *J. Atmos. Sci.*, **45**, 1285–1303.

Marécal, V., D. Hauser, and F. Roux, 1993.   The 12/13 January 1988 narrow cold-frontal rainband observed during MFDP/FRONTS 87.   Part II: Microphysics. *J. Atmos. Sci.*, **50**, 975–997.

Roux, F., 1985.   Retrieval of thermodynamic fields from multiple-Doppler radar data using the equations of motion and the thermodynamic equation. *Mon. Wea. Rev.*, **113**, 2142–2157.

Roux, F., 1988.   The west African squall line observed on 23 June 1981 during COPT 81: kinematics and thermodynamics of the convective region. *J. Atmos. Sci.*, **45**, 406–426.

Roux, F., and J. Sun, 1990.   Single-Doppler observations of west African squall line on 27–28 May 1981 during COPT 81: kinematics, thermodynamics and water budget. *Mon. Wea. Rev.*, **118**, 1826–1854.

Roux, F., J. Testud, M. Payen, and B. Pinty, 1984.   West African squall-line thermodynamic structure retrieved from dual-Doppler radar observations. *J. Atmos. Sci.*, **41**, 3104–3121.

Sun, J., and R.A. Houze, 1991.   Application of a thermodynamic retrieval technique to a numerical model. *Preprints of 25th Conference on Radar Meteorology*, American Meteorological Society, 131–134.

Sun, S., and H. Uyeda, 2001.   Three-dimensional retrieval of microphysical and thermodynamic variables in snow cloud: A case of January 23, 1992. *Submitted to J. Meteor. Soc. Japan.*

Xue, M., K.K. Droegemeier, V. Wong, A. Shapiro, and K. Brewster, 1995.   *Advanced regional prediction system ARPS user's guide*, Center for Analysis and Prediction of Storms, the University of Oklahoma, 380 pp.